



Article

Ionospheric Correction of L-Band SAR Interferometry for Accurate Ice-Motion Measurements: A Case Study in the Grove Mountains Area, East Antarctica

Yuanyuan Ma ^{1,2,3}, Zemin Wang ^{1,3,*}, Fei Li ^{1,2,3}, Shunlun Liu ^{1,3}, Jiachun An ^{1,3} , Bing Li ^{1,4} and Weifeng Ma ⁵

¹ Chinese Antarctic Center of Surveying and Mapping, Wuhan University, Wuhan 430079, China; mayuanyuan123@whu.edu.cn (Y.M.); fli@whu.edu.cn (F.L.); shlliu@whu.edu.cn (S.L.); jcan@whu.edu.cn (J.A.); binglee@whu.edu.cn (B.L.)

² Electronic Information School, Wuhan University, Wuhan 430072, China

³ Key Laboratory of Polar Surveying and Mapping, MNR, Wuhan 430079, China

⁴ School of Mathematics & Computer Science, Wuhan Polytechnic University, Wuhan 430048, China

⁵ Faculty of Geography, Yunnan Normal University, Kunming 650050, China; 150020@ynnu.edu.cn

* Correspondence: zmwang@whu.edu.cn; Tel.: +86-27-6877-8030

Abstract: Ice motion is an essential element for accurately evaluating glacier mass balance. Interferometric synthetic aperture radar (InSAR) has been widely applied for monitoring ice motion with high precision and wide coverage in the Antarctic. However, the ionospheric effects can significantly impact InSAR-based ice-motion measurements. At low radar frequencies in particular, the ionospheric effects have been regarded as a serious source of noise in L-band SAR data. The split-spectrum method (SSM) is commonly used for correcting the ionospheric effects of the InSAR technique. However, it requires spatial filtering with the relatively large factors used to scale the sub-bands' interferograms, which often results in an unwrapped phase error. In this paper, a reformulation of the split-spectrum method (RSSM) is introduced to correct the ionospheric effects in the Grove Mountains of East Antarctica, which have slow ice flow and frequent ionosphere changes. The results show that RSSM can effectively correct the ionospheric effects of InSAR-based ice-motion measurements. To evaluate the ability of ionospheric correction using RSSM, the result of ionospheric correction derived from SSM is compared with the results of RSSM. In addition, ionosphere-corrected ice motion is also compared with GPS and MEaSURES. The results show that the ionosphere-corrected ice velocities are in good agreement with GPS observations and MEaSURES. The average ice velocity from the InSAR time series is compared to that from MEaSURES, and the average ionosphere-corrected ice velocity error reduces 43.9% in SSM and 51.1% in RSSM, respectively. The ionosphere-corrected ice velocity error is the most significant, reducing 86.9% in SSM and 90.4% in RSSM from 1 November 2007 to 19 December 2007. The results show that the ability of RSSM to correct ionospheric effects is slightly better than that of SSM. Therefore, we deduce that the RSSM offers a feasible way to correct ionospheric effects in InSAR-based ice-motion measurements in Antarctica.

Keywords: glacier mass balance; SAR interferometry; ice motion; ionospheric effects; reformulation of the split-spectrum method; ionospheric correction



Citation: Ma, Y.; Wang, Z.; Li, F.; Liu, S.; An, J.; Li, B.; Ma, W. Ionospheric Correction of L-Band SAR Interferometry for Accurate Ice-Motion Measurements: A Case Study in the Grove Mountains Area, East Antarctica. *Remote Sens.* **2022**, *14*, 556. <https://doi.org/10.3390/rs14030556>

Academic Editors: Xiao Cheng, Zhaohui Chi and Yan Liu

Received: 20 November 2021

Accepted: 17 January 2022

Published: 25 January 2022

Publisher's Note: MDPI stays neutral with regard to jurisdictional claims in published maps and institutional affiliations.



Copyright: © 2022 by the authors. Licensee MDPI, Basel, Switzerland. This article is an open access article distributed under the terms and conditions of the Creative Commons Attribution (CC BY) license (<https://creativecommons.org/licenses/by/4.0/>).

1. Introduction

The working Group I report of the Sixth Assessment Report (AR6) of the Intergovernmental Panel on Climate Change (IPCC) was released in August 2021. AR6 indicates that the components of the cryosphere have rapidly been shrinking under climate warming over recent years. The rapid shrinking of the cryosphere makes it the most significant potential contributor to rising global mean sea levels [1,2]. Ice motion is a fundamental observation required to predict the behavior of the cryosphere and global climate change in the future [3,4]. Large-scale ice-motion measurements in Antarctica are vital for determining the mass balance of ice sheets [5]. In recent years, many remote-sensing techniques

have allowed for the measurements of glacial movements over large areas, making them an indispensable tool for monitoring ice motion in Antarctica [6,7]. To monitor ice motion based on SAR images, phase- or offset-based means can be applied [8,9]. Phase-based methods include differential interferometric SAR, while offset-based methods can be classified into the speckle-tracking (ST) method and the feature-tracking (FT) method [10]. They have all been widely applied in ice-motion measurements in Antarctica [11,12].

The ST method is based on the cross-correlation of the coherence of the broad-band speckle-noise pattern and uses this to calculate ice motion from differential SAR data pairs [13]. The FT method is also based on this cross-correlation and only depends on image features. The ST and FT have more robustness for regions of fast flow, especially in the outlet glaciers, where InSAR techniques may be difficult to unwrap because of low coherence [8,14]. One drawback of them, however, is that their resolution is limited by the need to cross-correlate patches with widths of several tens of pixels [7,8]. Compared with ST and FT, InSAR techniques have been applied to monitor ice motion from phase differences between repeated SAR acquisitions [7,13]. The InSAR techniques are used for periodic observations of ice motion over long time intervals with large experimental areas [15]. Although InSAR techniques only obtain radar line-of-sight (LOS) signals, they can provide higher accuracy and better spatial resolution. In areas of the slow flow of ice motion, such as the Grove Mountains area in the Chinese PANDA section of East Antarctica, with a maximum ice velocity of 40 m/yr, InSAR-based ice velocity estimates showed much better results than ST or FT [16,17].

Accurate ice-motion measurements are also critical for constraining ice-sheet models and a better understanding of their movement mechanisms. However, L-band InSAR ice-motion measurements have been severely influenced by ionospheric disturbances [18]. The ionospheric effects are included by phase advance, phase or amplitude scintillation, and Faraday rotation in the interferometric phase [19,20]. In Antarctica in particular, ionospheric fluctuations are very active. The ionospheric signal varies between InSAR image acquisition time and can bring the ionospheric effects into the interferograms, which serve as a source of noise for InSAR-based measurements [17]. Recent studies show that the ionospheric effects can cause an average of 17 m/yr and 8 m/yr errors in ST-based ice velocity estimated from L-band SAR images in West Antarctica and East Antarctica, respectively [10]. In Greenland and Antarctica, ionospheric errors reach 14 m/yr and 10 m/yr in InSAR-based ice motion measurements, respectively, which makes it difficult to analyze the mechanism of ice motion [13]. The estimation of the ionospheric phase is, therefore, a vital step in removing ionospheric effects from interferograms and improving the accuracy of InSAR-based ice-motion measurements [21,22].

Recently, several methods have been introduced to remove ionospheric effects from InSAR measurements [20,23]. The range group-phase delay method calculates the ionospheric phase based on the range shift between SAR images [24] and the accuracy is closely related to the quality of the SAR image coregistration in the range direction [25]. ALOS-1 PALSAR, however, has a low range resolution, and this limits the development of the range group-phase method. The Faraday rotation method can be estimated by absolute ionosphere total electron content (TEC) according to full-polarization SAR images [25]. However, in Antarctica, the number of full-polarization SAR images is very small, which limits the application of this method; the split-spectrum method (SSM) is considered the most responsible approach to estimating the ionospheric phase [26,27]. The concept of the SSM is to determine separate interferograms for spectral sub-bands, permitting separation of the dispersive and the nondispersive phase components [27,28]. One of the disadvantages is, however, that spatial filters can easily result in phase differences of 0.1 radians or more [29]. In this paper, we employ a reformulation of the split-spectrum method (RSSM) to remove the ionospheric effects from InSAR ice-motion measurements in the Grove Mountains of East Antarctica. RSSM estimates the ionospheric effects by utilizing a split-spectrum double-difference interferometric phase and a full-bandwidth differential interferometric phase [29]. On the one hand, RSSM only scales necessarily the unwrapped

split-spectrum double-difference interferometric phase with a large coefficient. On the other hand, the full-bandwidth interferogram was used for ionospheric estimation instead of the sub-band interferogram. Those reformulated steps increase the robustness of the unwrapping and filtering [29].

We present the SSM and RSSM to estimate and correct the ionospheric effects for SAR interferograms. Section 2 restates the main content of SSM and RSSM for InSAR ionospheric correction with an emphasis on ice-motion measurement. Section 3 introduces the materials and implementation. A selected case study using L-band ALOS PALSAR in the Grove Mountains area of East Antarctica is given to analyze the significance of ionospheric effects for ice-motion measurements. An overall process of the implementation of the SSM and the RSSM is summarized, and its key procedures are analyzed in detail. Section 4 presents the experimental results of the ionospheric correction based on the SSM and the RSSM. The abilities of ionospheric correction using the RSSM in InSAR-based ice-motion measurements are discussed in Section 5. Section 6 gives our conclusion on ionospheric correction for ice motion in Antarctica, and a future research plan is briefly introduced.

2. Methodology

2.1. Ionospheric Effects on SAR Interferometry

For repeat-pass SAR data in the same area, due to different acquisition times of SAR interferometry pairs, different data are subject to different ionospheric effects. Those effects lead to localized phase features in SAR interferograms [30]. The ionosphere is active with fast spatial and temporal changes in Antarctica, where the ionospheric effects are relatively large than that of midlatitudes [31]. InSAR-based ice motion measurements are disturbed by the azimuth shift and ionospheric effects. The ionospheric effects are mixed in the SAR interferometry phase, which needs to be eliminated from the SAR interferograms [20,32]. The repeat-pass InSAR interferograms ($\Delta\varnothing$) formed from two SAR acquisitions at different times contain different components as follows:

$$\Delta\varnothing = \varnothing_{displacement} + \varnothing_{topographic} + \varnothing_{ionosphere} + \varnothing_{flat} + \varnothing_{atmosphere} + \varnothing_{orbit} \quad (1)$$

where the topographic phase, $\varnothing_{topographic}$, and the flat-earth phase, \varnothing_{flat} , are subtracted from the interferograms using the Bedmap2 DEM [33]. A polynomial baseline-fitting method is applied to mitigate the phase distortion (\varnothing_{orbit}) related to orbit errors [34]. Moreover, baseline fitting can also help in compensating for tropospheric and ionospheric phase distortion. However, this alone is not sufficient to remove the ionospheric phase ($\varnothing_{ionosphere}$). Therefore, it is still essential to implement ionospheric correction first before performing baseline fitting, as the correct order of ionospheric correction and baseline fitting can avoid repeated removal of the ionospheric phase [13]. In addition, atmospheric delay ($\varnothing_{atmosphere}$) is not considered in our study.

The SSM [35,36] exploits the dispersive property of $\varnothing_{ionosphere}$ to correct ionospheric effects from SAR interferometry, and the ionospheric phase belongs to the dispersive component [26,37]. The SSM makes use of the dispersive feature of the ionosphere, by using slightly different center frequencies for the sub-band interferograms [38]. Usually, the sub-band interferogram is 1/3 of the full-band interferogram for high estimation accuracy [19,39]. The linear-equation system can deal with dispersive ionospheric phase, $\varnothing_{ionosphere}$, according to:

$$\varnothing_{ionosphere} = \frac{f_2}{f_0} \frac{f_1 f_2}{(f_2^2 - f_1^2)} \varnothing_1 - \frac{f_1}{f_0} \frac{f_1 f_2}{(f_2^2 - f_1^2)} \varnothing_2 \quad (2)$$

where \varnothing_1 and \varnothing_2 represent the interferometric phase corresponding to sub-bands with center frequencies of f_1 and f_2 , respectively. f_0 is the frequency of the full-bandwidth interferometric phase \varnothing_0 .

If \varnothing_1 and \varnothing_2 are sub-band interferograms with equal bandwidth, it is suitable to suppose that \varnothing_1 and \varnothing_2 have the same statistical distribution (i.e., $\sigma(\theta_1) = \sigma(\theta_2)$). Under the circumstances, the accuracy of the ionospheric estimation is [13,40]:

$$\text{std}(\varnothing_{\text{ionosphere}}) = \sqrt{1 + \left(\frac{f_1}{f_2}\right)^2 \frac{f_2}{f_0} \frac{f_1 f_2}{(f_2^2 - f_1^2)} \frac{1}{\sqrt{2N_b}} \frac{\sqrt{1 - \gamma_{\text{sub-band}}^2}}{\gamma_{\text{sub-band}}}} \quad (3)$$

where $N_b = P_N \times B_{\text{sub-band}} / B_{\text{full-band}}$ is the number of independent looks in the multi-looked sub-bands interferogram. P_N is the number of looks in the full-band interferogram. $B_{\text{sub-band}}$ and $B_{\text{full-band}}$ are the sub-band and full-band bandwidth of the SAR image, respectively. $\gamma_{\text{sub-band}}$ is the sub-band interferometric coherence. It can be inferred that the accuracy of the ionospheric phase estimation is determined by the frequency and the coherence of the sub-band interferograms.

2.2. The Reformulated Split-Spectrum Method (RSSM)

Equation (2) can be slightly reformulated as a linear combination of the full-bandwidth interferograms phase \varnothing_0 and the split-spectrum double differential phase ($\varnothing_2 - \varnothing_1$) [29].

$$\varnothing_{\text{reionosphere}} = \frac{f_1 f_2}{f_0(f_2 + f_1)} \varnothing_0 - \frac{f_1 f_2}{2f_0(f_2 - f_1)} (\varnothing_2 - \varnothing_1) \quad (4)$$

The accuracy of the ionosphere is calculated as:

$$\text{std}(\varnothing_{\text{reionosphere}}) = \sqrt{\left(\frac{f_1 f_2}{f_0(f_2 + f_1)}\right)^2 (\text{std}(\varnothing_{\text{full-band}}))^2 + 2\left(\frac{f_1 f_2}{2f_0(f_2 - f_1)}\right)^2 (\text{std}(\varnothing_{\text{sub-band}}))^2} \quad (5)$$

The full-band interferogram accuracy can be estimated as:

$$\text{std}(\varnothing_{\text{full-band}}) = \frac{1}{\sqrt{2P_N}} \frac{\sqrt{1 - \gamma_{\text{full-band}}^2}}{\gamma_{\text{full-band}}} \quad (6)$$

where $P_N = 3N_b$, and $\gamma_{\text{full-band}}$ is the full-band interferometric coherence [41]. It can be seen that the accuracy of the ionospheric phase estimate mainly relies on the frequency and the coherence of the full-band and sub-band interferograms. It is supposed that the coherences of $\varnothing_{\text{sub-band}}$ and $\varnothing_{\text{full-band}}$ are equal (i.e., $\gamma_{\text{full-band}} = \gamma_{\text{sub-band}}$). Under this assumption, the relationship between the accuracy of the sub-band and full-band interferogram is:

$$\text{std}(\varnothing_{\text{full-band}}) = \text{std}(\varnothing_{\text{sub-band}}) / \sqrt{3} \quad (7)$$

The ionospheric phase accuracy, from (5) and (7), is

$$\text{std}(\varnothing_{\text{reionosphere}}) = \sqrt{\frac{1}{3} \left(\frac{f_1 f_2}{f_0(f_2 + f_1)}\right)^2 + 2 \left(\frac{f_1 f_2}{2f_0(f_2 - f_1)}\right)^2} \text{std}(\varnothing_{\text{sub-band}}) \quad (8)$$

2.3. Compare Accuracy between SSM and RSSM

According to the different sub-bands ($f_1 = f_0 - \Delta f$; $f_2 = f_0 + \Delta f$), we can deduct that the ratio of the accuracy of SSM and RSSM is given by:

$$\frac{\text{std}(\varnothing_{\text{ionosphere}})}{\text{std}(\varnothing_{\text{reionosphere}})} = \sqrt{\frac{\left(\left(1 + \left(\frac{f_1}{f_2}\right)^2\right) \frac{f_2}{f_0} \frac{f_1 f_2}{(f_2^2 - f_1^2)}\right)^2}{\frac{1}{3} \left(\frac{f_1 f_2}{f_0(f_2 + f_1)}\right)^2 + 2 \left(\frac{f_1 f_2}{2f_0(f_2 - f_1)}\right)^2}} = \sqrt{\frac{3(f_0)^2 + 3(\Delta f)^2}{3(f_0)^2 + 2(\Delta f)^2}} > 1 \quad (9)$$

From Equation (9), we can see that the ratio of the accuracy of SSM and RSSM is greater than one. To offer a reliable performance analysis of ionospheric correction, we compare the standard deviations of the theoretical ionospheric estimate using SSM and RSSM. The relationship between the ionospheric-phase standard deviation (STD) and coherence is shown in Figure 1. The theoretical ionosphere is estimated using SSM as derived from Equation (3) and RSSM as derived from Equation (8). We see that the STD of RSSM is slightly lower than SSM in low coherence areas (coherence < 0.4), and both are nearly the same in high coherence areas (coherence > 0.4). We can thus infer that the ionospheric-phase estimate using RSSM is slightly better than SSM in Antarctica with low coherence.

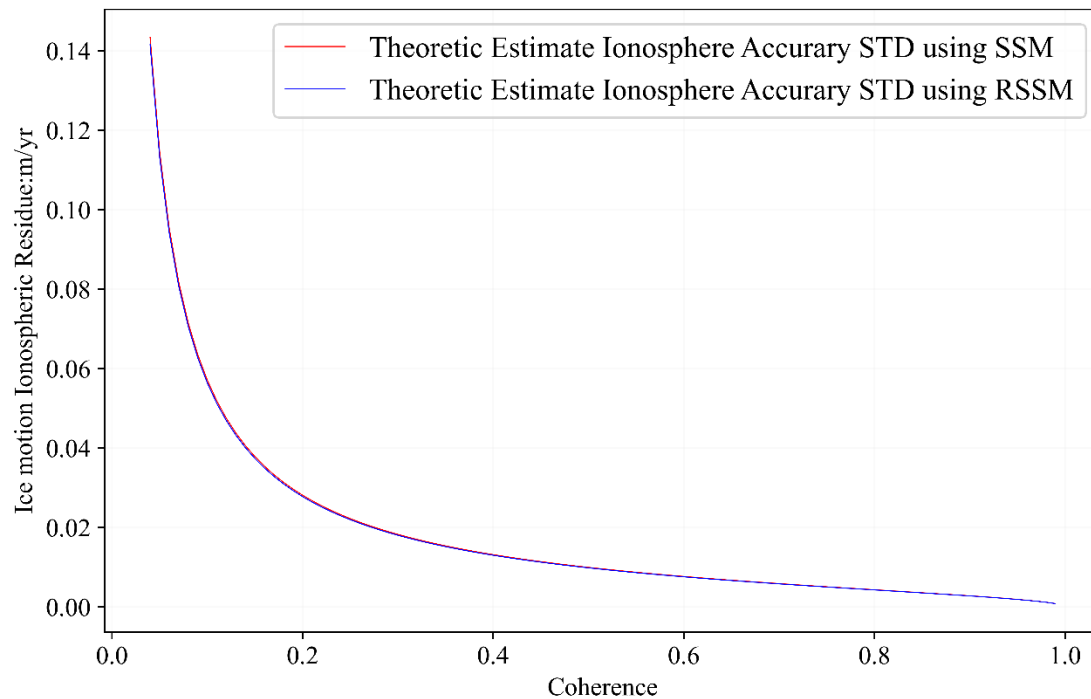


Figure 1. Comparison of the theoretical residuals between RSSM and SSM estimates of ionosphere ice motion. The X-axis is the interferometric coherence, while the Y-axis is the ice motion ionosphere residue.

3. Materials and Implementation

3.1. Datasets and Study Area

ALOS-1 PALSAR is an L-band SAR dataset with a revisit time of 46 days. The L-band SAR data are less influenced by ice motion than the C-band and X-band SAR data because their waves penetrate deeper into the surface and temporal coherence is higher [42]. In our study, a track-long of ALOS-1 PALSAR is applied to analyze the abilities of the ionospheric correction using the SSM and RSSM. We selected the Grove Mountains area as the experimental areas, where the ionosphere changes with fast spatial and temporal changes [13]. Details about the data are shown in Table 1. We also used ice-velocity measurements by GPS and MEaSURES to validate our results.

Figure 2 illustrates the coverage and map projection of the ALOS PALSAR images. The SAR images cover the Grove Mountains area located in Princess Elizabeth Land, East Antarctica, where the ionosphere is very active with fast spatial and temporal changes. The Grove Mountains area has elevations ranging from 1800 to 2100 m a.s.l., which decrease from southeast to northwest [43]. The Grove Mountains area is about 400 km away from the Antarctic Zhongshan station (China). The eastern flank of the Lambert–Amery ice shelf is close to the experimental area [44], and the ice from the Antarctic inland flows through the Grove Mountains to the Lambert–Amery ice shelf along the northwest direction, and the motion is relatively slow and maximum ice velocity reaches 40 m/yr [45]. Therefore,

slower ice velocities can be monitored with the InSAR techniques. Furthermore, the Grove Mountains are also a special area in East Antarctic that involves sixty-four isolated Nunataks (as shown in Figure 2a), which can offer many stable reference points.

Table 1. ALOS PALSAR data information of application on the experiment.

Experiment Area	Track No.	Frame	Reference	Secondary	SLC Numbers	Temporal Baseline
Grove Mountains	583	5590–5650	16 September 2007	1 November 2007	7	46 days
Grove Mountains	583	5590–5650	1 November 2007	17 December 2007	7	46 days
Grove Mountains	583	5590–5650	3 November 2008	19 December 2008	7	46 days
Grove Mountains	583	5590–5650	24 September 2010	9 November 2010	7	46 days
Grove Mountains	583	5590–5650	9 November 2010	25 December 2010	7	46 days

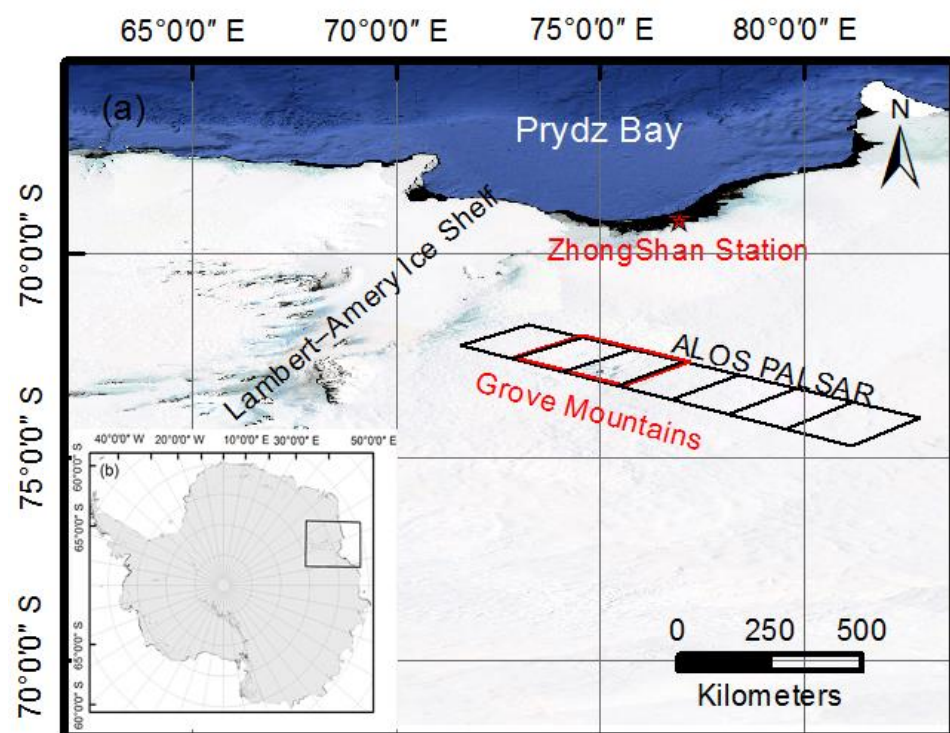


Figure 2. The coverage and map projection of ALOS PALSAR images (a) and the location of the Grove Mountains area (b). The black rectangle in (b) shows the black box in (a). The red rectangle and red pentacle indicate the Grove Mountains areas and the Zhongshan station, respectively.

3.2. Data Processing Using SSM and RSSM

The InSAR ionospheric correction of the ALOS PALSAR processing workflow is generalized (Figure 3). Here follows the explanation of the applied implementation of the SSM and RSSM.

The reference and secondary images needed to be precisely coregistered; in our implementation, all images used speckle-tracking techniques to register them [46]. Precise register needed to be ensured due to the spatial changes of the pixel movement caused by the ice motion and massive ionospheric azimuth variations. Regular InSAR coregistration steps were applied as usual for the fine registration. We also used the polynomial-fitted offset from the above registration to perform the final registration. Moreover, the secondary images were resampled using the shifts that were calculated during the fine registration [13]. The Bedmap2 DEM was applied to remove the topographic phase from the full-band and sub-band interferograms [33]. We conducted band-pass filtering in the range to create two sub-band images. After resampling, the full-band and sub-band interferograms

were calculated with the fine offset from the above fine registration. The amount of multilooking is discussed in Section 4. A minimum-cost-flow algorithm was used for all the interferograms' unwrapping. The ionospheric phase was computed by SSM and RSSM. The computed ionospheric phase had to be strongly smoothed to eliminate outliers and suppress noise. We used a recursive phase-unwrapping-correcting method to decrease phase unwrapping errors [13], and a median filter to suppress the computed ionospheric phase noise. Pixels with a difference greater than a threshold (3σ , σ estimate based on Equations (3) and (8)) acted as outliers and were removed. In addition, we also used an isotropic 2D Gaussian filter to eliminate random noise. The abnormal ionospheric phase changes frequently, usually resulting in a high-fringe density in the interferogram. A conventional isotropic-filter kernel may lead to errors in areas of high-fringe density or near the margins of the interferograms [19]. Hence, we implemented an adaptive edge-preserving filter to solve this issue [38].

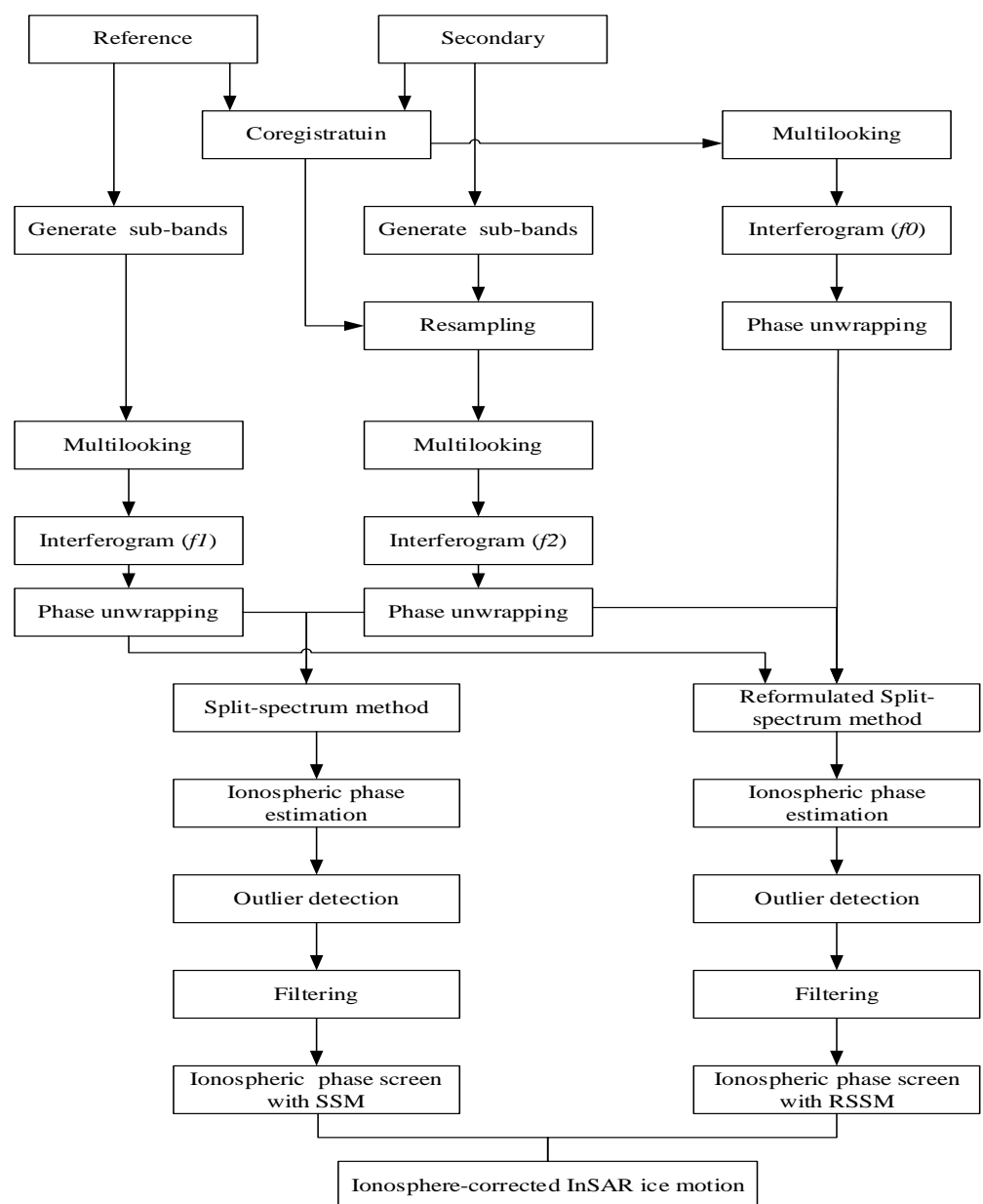


Figure 3. Data process of the ionospheric-phase estimation and correction for ALOS PALSAR.

Finally, the ionospheric effects were removed from the original interferograms by Equation (1). The ionosphere-corrected InSAR ice motion was verified by ice velocity from GPS and MEaSURES.

4. Results

4.1. Ionospheric-Phase Estimation

Ionospheric-phase estimation is an important prerequisite for the process of ionosphere-corrected InSAR ice-motion measurement. Before the estimation, the SAR images are processed by a multilooking operation of 18 (range) \times 12 (azimuth) to reduce speckle noise. We generate differential ionospheric-phase screens with differential methods. Ionospheric-phase estimation using the SSM and the RSSM followed the procedures described in Section 3.2; those phases are referred to as the “Ionosphere-phase estimation using SSM” and “Ionosphere-phase estimation using RSSM”, respectively. The comparisons are shown in Figure 4. We find that the ionospheric-phase bias between SSM and RSSM were in the internal $(-\pi, \pi)$.

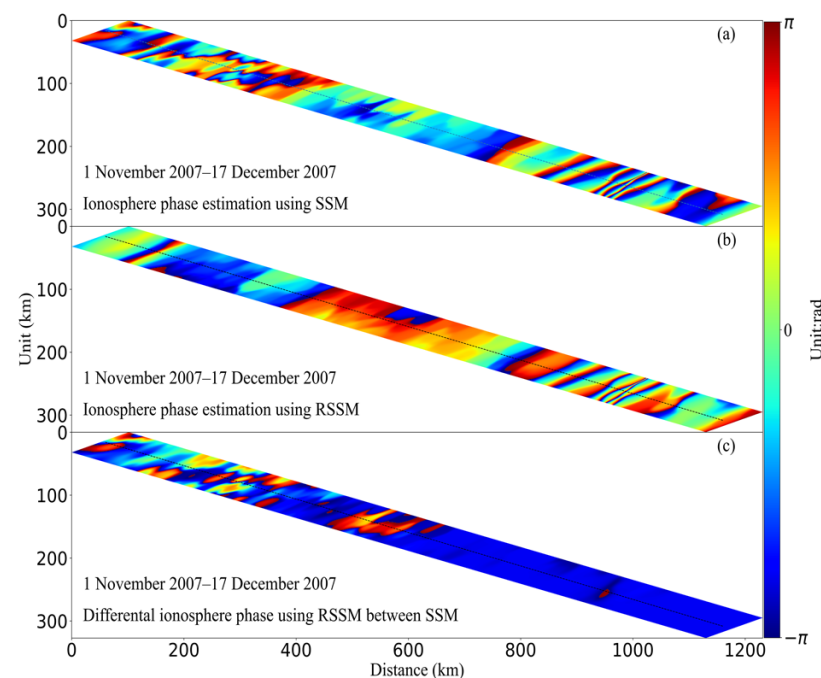


Figure 4. ALOS PALSAR data ionospheric estimation result. (a) Ionospheric phase (wrapped) estimated using SSM. (b) Ionospheric phase (wrapped) estimated using RSSM. (c) The ionospheric-phase bias between SSM and RSSM.

To compare the accuracy of the ionospheric-phase estimation using SSM and RSSM, we calculated the mean and standard deviation of the ionospheric-phase estimate using SSM and RSSM. The mean and standard deviation of the ionospheric phase (unwrapped) are shown in Table 2. We find that the mean and standard deviation of the ionospheric phase using RSSM is less than when using SSM. Therefore, we conclude that RSSM is more suitable for ionosphere-corrected InSAR ice-motion measurements than SSM.

Table 2. Comparison of the mean and standard deviation of the ionospheric phase by SSM and RSSM.

Methods	The Mean of the Ionospheric Phase Screen (Rad)	The Standard Deviation of the Ionospheric-Phase Screen (Rad)
SSM	−23.5	30.8
RSSM	−21.1	28.2

4.2. Ionospheric-Phase Correction

When the ionospheric-phase estimation is complete, the ionospheric effects within the SAR interferometric phase need to be corrected in the steps. We apply the ionospheric correction and baseline-fitting steps within the topography-phase-removed interferograms and obtained the original interferogram without the ionospheric correction, as shown in Figure 5a, the ionosphere-corrected interferogram with ionospheric correction using SSM, as shown in Figure 5b, and the ionosphere-corrected interferogram with ionospheric correction using RSSM, as shown in Figure 5c.

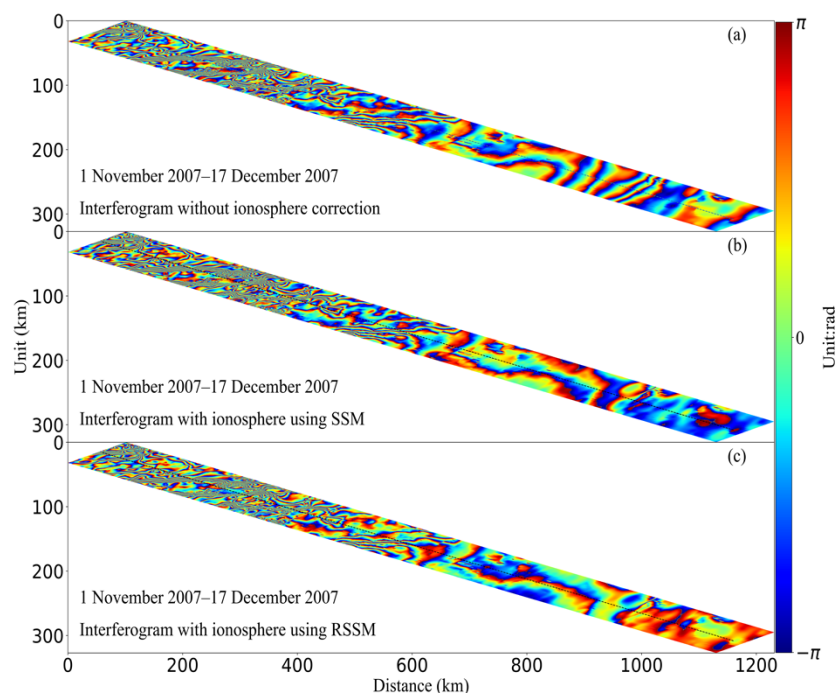


Figure 5. ALOS PALSAR images' ionospheric correction results. (a) Interferogram without ionospheric correction. (b) Interferogram with ionospheric correction using SSM. (c) Interferogram with ionospheric correction using RSSM. We can distinguish phases related to ice motion and the ionosphere from Figure 5a,b.

To assess the ionospheric correction performance, we compare the profiles of the ice velocity with the ionospheric correction using SSM and RSSM, as extracted from Figure 4a,b, and the profiles are presented in Figure 6a. The interferogram without ionospheric correction (Figure 5a) and the interferograms with ionospheric correction using SSM (Figure 5b) and RSSM (Figure 5c), along with their profiles, are displayed in Figure 6b.

Figure 6a shows that the ionospheric effects lead to significant local biases in apparent ice motion. When comparing ice velocity caused by the ionospheric effects using SSM and RSSM, we find that the former is less than the latter. Figure 6b indicates that the ionospheric effect causes peak-to-peak ice-velocity errors of 6.4 m/yr using SSM and 6.9 m/yr using RSSM. In addition, we also find that in the relatively slow-moving parts of the profile along this interferogram, the ionospheric effects are larger than the ice-motion signal itself, which highlights the necessity of ionospheric correction in the ice-motion measurements based on L-band SAR data.

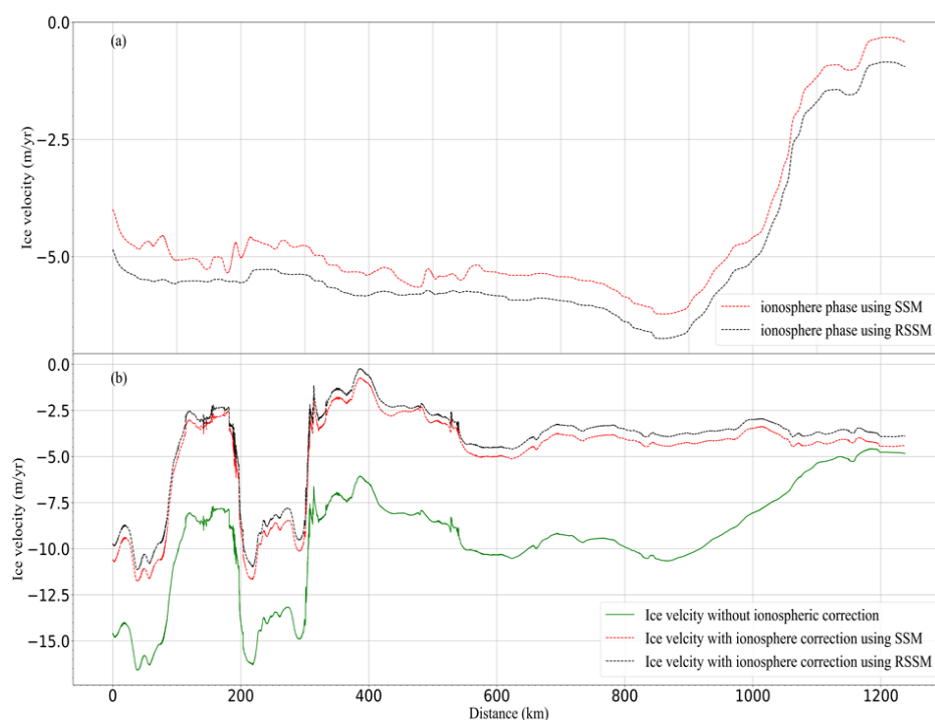


Figure 6. ALOS PALSAR images ionospheric correction result profile analysis. (a) Ionospheric-signal estimation using SSM (red dash curve) and ionospheric-signal estimation using RSSM (black dash curve) extracted from Figure 4a,b, respectively. (b) Ice velocity without ionospheric correction (green solid curve) and with ionospheric correction using SSM (red solid curve) and with ionospheric correction RSSM (black solid curve) extracted from Figure 5a–c, respectively.

5. Discussion

As mentioned above, SSM and RSSM are used to estimate the ionospheric phase and correct the ionospheric effects of InSAR. Therefore, here we will discuss the ability of the ionosphere-corrected InSAR ice-motion measurements using RSSM by comparing them with SSM and GPS and MEaSURES. GPS and MEaSURES ice velocity have been used to validate the accuracy of ionosphere-corrected InSAR ice-motion measurements and to emphasize the advantages of RSSM.

5.1. Comparison with GPS

The Chinese Antarctic research team conducted GPS observations of the Grove Mountains from 17 January 2006 to 31 January 2006 and obtained high-accuracy GPS ice velocity data. To validate the abilities of the ionospheric correction for InSAR-based ice-motion measurements, we compared the InSAR-based ice velocity with GPS-based ice velocity [16,47]. Seven GPS measurements were used for the validation. For each GPS-monitoring point, the InSAR-monitoring point located near the GPS point within a horizontal distance of ≤ 50 m were selected to enable the comparison. Table 3 shows that the difference between GPS measurements and ice-velocity measurements without ionospheric correction and with the ionospheric correction using SSM, RSSM, and the ALOS PALSAR data pair from Table 1. The root mean square (RMS) value of the ice velocities in the area was estimated. We find that the RMS of the differences dropped from 3.82 m/yr of the interferogram without ionospheric correction to 1.70 m/yr of the interferogram with the ionospheric corrections using SSM and 1.16 m/yr of the interferogram with the ionospheric corrections using RSSM. The improvement with ionospheric correction using SSM and RSSM are very large, and the latter is better than the former. But we also find that an obvious difference can be seen between GPS and ionosphere-corrected InSAR. This obvious difference may be attributed to three factors. The first factor is the spatial mismatch between the InSAR

measurement points and GPS monitoring points. A distance of a few tens of meters might cause significant changes in different monitoring points. The second factor is InSAR and GPS monitor ice flow in different directions. The third factor is the different times of observation between the InSAR and GPS. However, Envisat ASAR images (C-band) with DInSAR and offset-tracking methods have proved that ice velocities for the years 2006, 2007, and 2009 had no obvious interannual changes in the Grove Mountains [16,47]. Therefore, the difference between the InSAR and GPS caused by the different times of observation is very small [16].

Table 3. Comparison between GPS measurements and ice velocity without ionospheric correction and with ionospheric correction using SSM and RSSM.

Points	Latitude	Longitude	GPS	Ice Velocity (m/yr)					
				InSAR without Ionospheric Correction	Difference between GPS and InSAR	Ionospheric Correction InSAR Using SSM	Difference between GPS and SSM	Ionospheric Correction InSAR Using RSSM	Difference between GPS and RSSM
PLE1	72°51′02″	75°11′29″	3.54	6.51	−2.97	2.78	0.76	1.88	1.66
PLE2	72°52′41″	75°12′45″	1.11	5.01	−3.90	2.48	−1.37	1.57	−0.46
PLE3	72°51′10″	75°12′08″	0.62	4.85	−4.23	1.52	−0.90	1.09	−0.47
PLE4	72°50′10″	75°13′14″	5.98	8.99	−3.01	6.85	−0.87	5.45	0.53
PLE5	72°50′43″	75°14′31″	7.32	12.67	−5.35	9.72	−2.40	7.83	−0.51
PLE6	72°50′28″	75°11′05″	5.4	9.70	−4.30	7.69	−2.29	6.84	−1.44
PLE7	72°51′16″	75°15′02″	12.34	14.32	−1.98	10.08	2.26	10.04	2.30

5.2. Comparison with MEaSURES

Seven repeat acquisitions are usable for the selected ALOS PALSAR tracks in the Grove Mountains area (see Figure 1). In total, we obtain five repeated SAR interferograms during the period from 2007 to 2010. A detailed introduction about the five interferograms is in Table 1. All the datasets are processed following the procedures introduced in Section 3.2, and the time series interferograms without ionospheric correction; thus, the time-series interferograms with ionospheric correction using SSM and RSSM were attained.

Figure 7 shows that five original interferograms are influenced by the ionospheric effects with peak distortions of several tens of centimeters (most severe ionospheric distortions are seen in the 2007 dataset, where the ionospheric distortion led to ice-motion errors that can reach about 6.9 m/yr).

Applying ionospheric correction in five original interferograms using SSM and RSSM, we get the time series ionospheric phase (as shown in Supplementary Materials, Figures S1 and S2), and find that five interferograms have severe ionospheric effects in the research area. Moreover, the ionospheric distortion varies with spatial and temporal variations.

Applying the ionospheric phase correction to the original interferograms, we get the time-series, ionosphere-corrected interferograms using SSM (as shown in Supplementary Materials Figure S3), and the time-series, ionosphere-corrected interferograms using RSSM are shown in Figure 8. We can see that the remaining ice-motion signal after ionospheric correction in five interferograms shows a similar spatial pattern and similar magnitude, which suggests ice velocities were steady in the Grove Mountains area during 2007–2010.

To discuss the abilities of the ionospheric correction for the InSAR ice-motion measurements in the future, we compare the ionosphere-corrected ice velocity with MEaSURES ice velocity. The MEaSURES ice velocity over the entire continent of Antarctica used six SAR sensors (ALOS PALSAR, Envisat ASAR, ERS-1, ERS-2, RADARSAT-1 and RADARSAR-2) in the framework of the International Polar Year from 2007 to 2009, and its mosaic uses 1400 tracks representing more than 3000 orbits [10,14,48]. In addition, [16,42] illustrate that ice velocity does not have obvious interannual changes in the Grove Mountains. Therefore, the MEaSURES ice velocity has been regarded as a reliable reference to show the abilities of the ionospheric correction for InSAR ice motion measurements. We extract a profile along the center of the swath (white line in Figure S3 in the Supplementary Materials and

Figure 8) and plot the InSAR-based ice motion measurements without and with ionospheric correction using SSM and using RSSM for each multitemporal InSAR pair in Figure 9a–c. In addition, we also plot the MEaSUREs ice velocity in Figure 9.

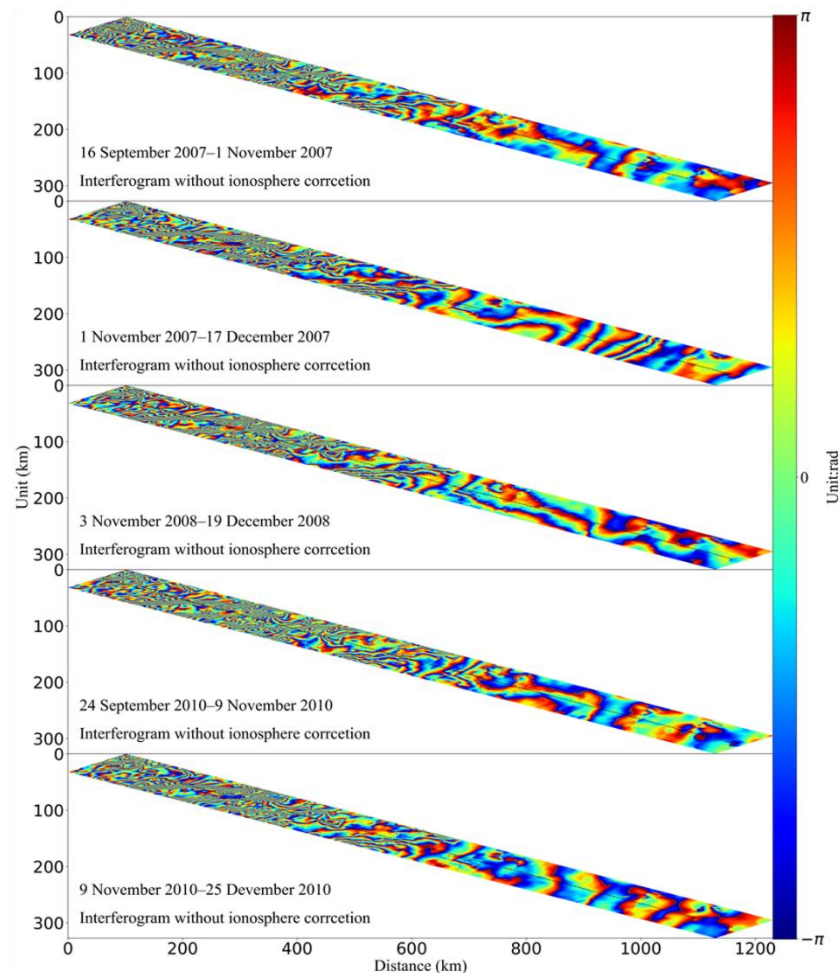


Figure 7. Time-series SAR Interferograms without ionospheric correction in Antarctica. The five original interferograms correspond to the five acquisition times in Table 1.

Without the ionospheric correction, the InSAR-based measurements deviate significantly from the MEaSUREs ice velocity and vary with time and space. Maximum deviations reach up to 6.9 m/yr from 1 November 2007 to 19 December 2007, as shown in Figure 9a. Compared with Figure 9a, we find that the InSAR-based measurements with ionospheric correction using SSM (Figure 9b) and RSSM (Figure 9c) match nicely with the MEaSUREs ice velocity. This agreement demonstrates that the ionospheric correction for ice motion can improve the accuracy of the InSAR-based ice-motion measurements. We also see that the matching degree of ionosphere-corrected with RSSM and MEaSUREs is better than that of ionosphere-corrected with SSM and MEaSUREs.

In addition, we calculated the measurement biases between ice velocity MEaSUREs and InSAR-derived time series ice velocity at different periods. The statistical histogram of the difference between time series ice velocity data and MEaSUREs ice velocity is shown in Figure 10a–e. We also averaged the time-series ice velocity without ionospheric correction converted from Figure 7 and average time-series ice velocity with ionospheric correction using SSM converted from Figure S3 (Figure S3 in the Supplementary Materials) and average time-series ice velocity with ionospheric correction using RSSM converted from Figure 8. The statistical histogram of the biases between average ice velocity and MEaSUREs ice velocity is shown in Figure 10f. Figure 10a–e show that the most significant

period of ionospheric correction is from 1 November 2007 to 19 December 2007, and the maximum drop is from 1.98 m/yr without correction to 0.26 m/yr with correction using SSM and 0.19 m/yr with correction using RSSM, corresponding to an 86.9% decrease in SSM and a 90.4% decrease in RSSM. Figure 10f shows that the standard deviation of the averaged ice velocity biases drops significantly after ionospheric correction was applied and that ionosphere-corrected InSAR ice velocity reduces biases relative to MEaSURES, a drop from 0.66 m/yr without correction to 0.37 m/yr with correction using SSM and 0.32 m/yr with correction using RSSM, corresponding to a 43.9% decrease in SSM and a 51.5% decrease in RSSM.

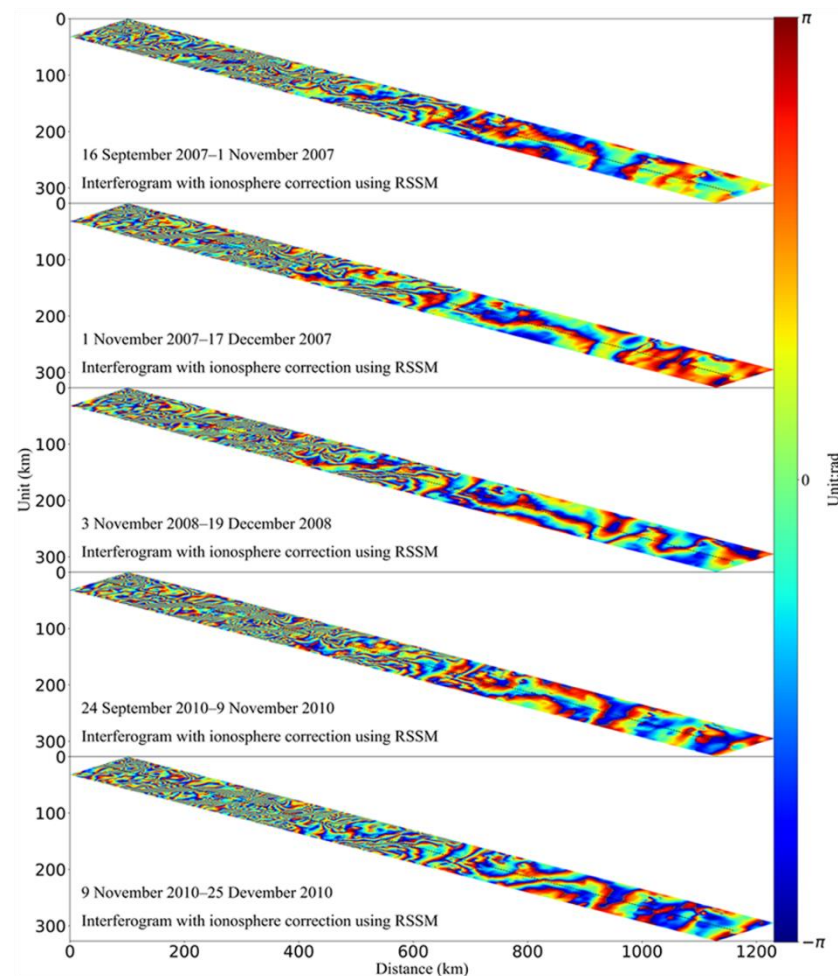


Figure 8. The time-series interferograms with ionospheric correction using the RSSM in Antarctica. The five interferograms for the five acquisition times are shown in Table 1.

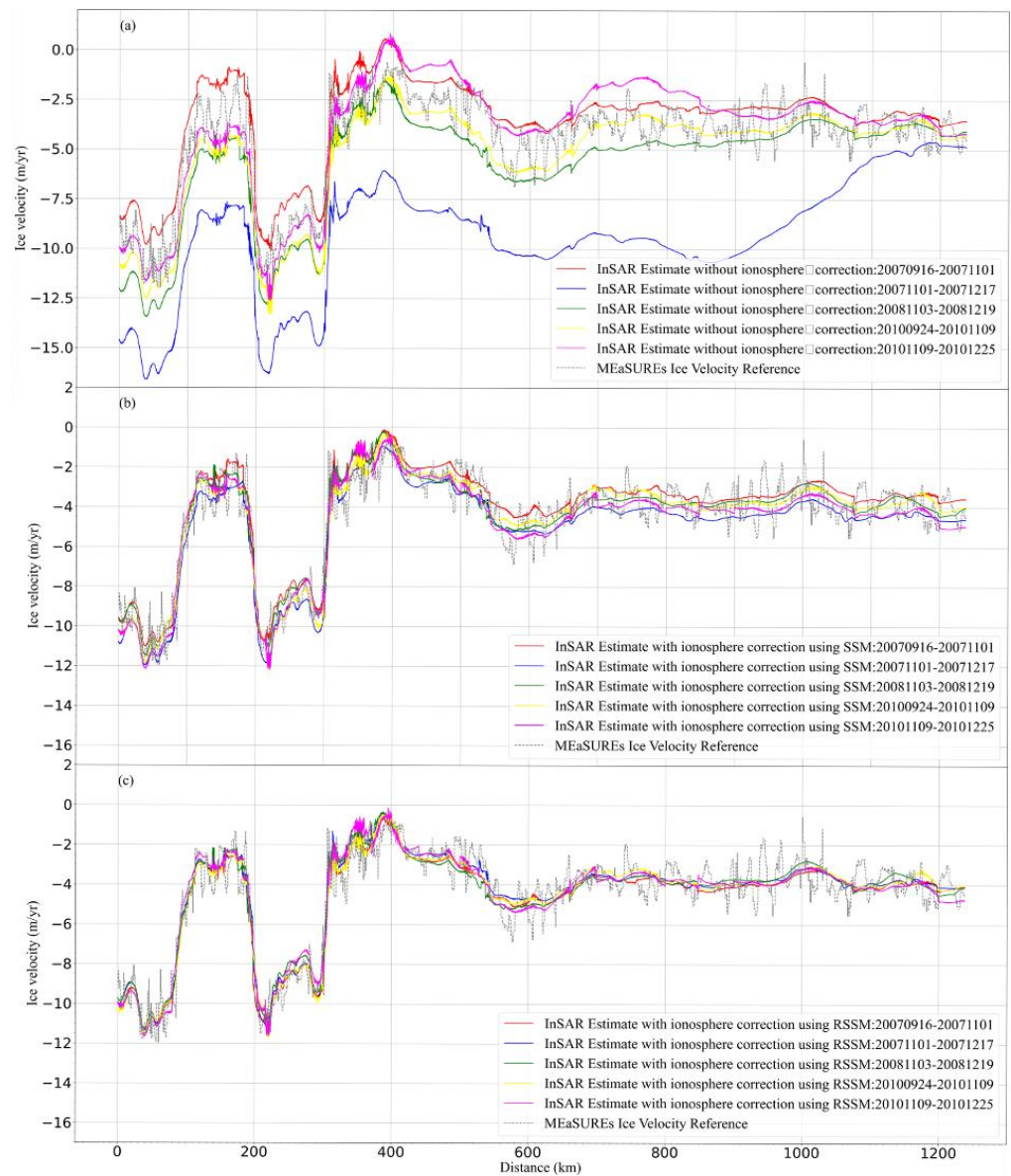


Figure 9. The time-series ice-velocity measurements profile analysis without ionospheric correction and with ionospheric correction using SSM and RSSM in Antarctica. (a–c): Reference ice velocity from MEaSUREs (gray) and InSAR-derived ice velocity measurements without ionospheric correction and with ionospheric correction using SSM and RSSM (other colors).

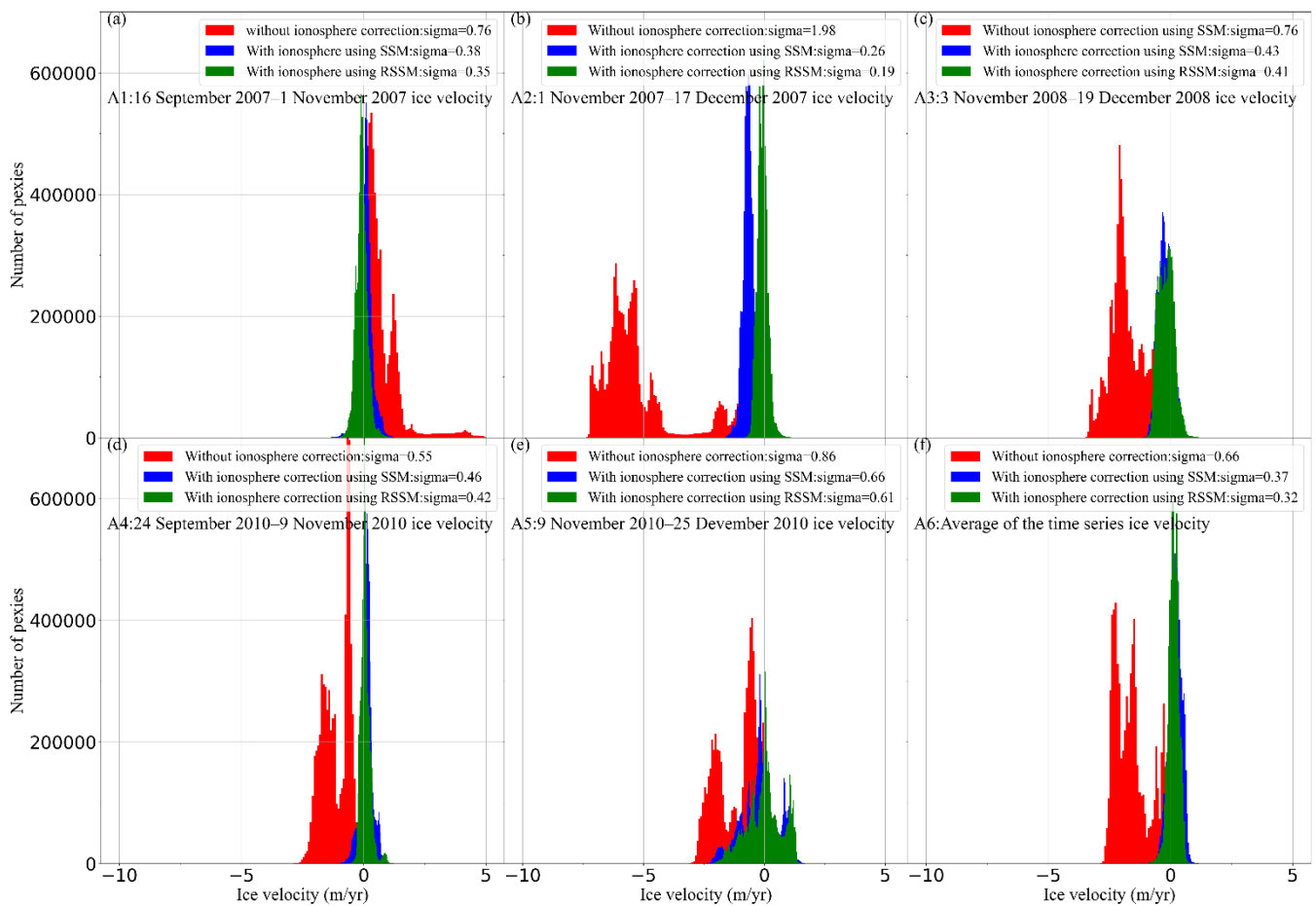


Figure 10. The statistical histogram of measurement biases between time-series ice velocity and MEaSURES ice velocity; (a) between A1 and MEaSURES; (b) between A2 and MEaSURES; (c) between A3 and MEaSURES; (d) between A4 and MEaSURES; (e) between A5 and MEaSURES; (f) between A6 and MEaSURES.

6. Conclusions

A large number of ALOS PALSAR data covering Antarctica are available for free download, which greatly facilitates the use of InSAR ice-motion measurements in Antarctica, but the ionospheric effects restrain its abilities and development, especially in regions with slow ice motion. In this paper, we present the RSSM for the correction of ionospheric effects in SAR interferograms. Our study area, located in the Grove Mountains where ionospheric disturbances occur frequently, was used to demonstrate the ability of RSSM by comparing ice-motion measurements without and with ionospheric correction using SSM and RSSM. The results of the experiment show that SSM and RSSM can effectively correct the ionospheric effects of InSAR in Antarctica and increase the accuracy of ionosphere-corrected InSAR measurements.

Comparing GPS-based ice velocity, we find that the RMS of the difference between GPS and InSAR drop from 3.82 m/yr without ionospheric correction to 1.70 m/yr with ionospheric correction using SSM and 1.16 m/yr with ionospheric correction using RSSM. In addition, we compare ice velocity between InSAR and MEaSURES. In all cases, we also find that ionospheric correction leads to significantly reduced biases and improves InSAR-based ice motion by a standard deviation reduction of 43.9% with the SSM and 51.5% with the RSSM. In summary, our study illustrates that RSSM is slightly better than SSM at correcting ionospheric effects from the InSAR-based ice motion in Antarctica.

Adding ionospheric correction to existing ice-motion approaches should be considered. Our study finds that ionospheric effects in ice-motion measurements can reach up to 6.9 m/yr in the Grove Mountain area. Those errors make ice-motion analysis from InSAR-based measurements more difficult. Hence, applying the ionospheric correction is of great importance to yield accurate ice-velocity information. Our future research will focus on the ionospheric correction of the C-band SAR interferogram (such as Sentinel-1A/B), which will reduce the ionospheric noise in ice-motion InSAR-based measurements in Antarctica.

Supplementary Materials: The Supplementary Materials are available online at <https://www.mdpi.com/article/10.3390/rs14030556/s1>.

Author Contributions: Z.W. and Y.M. developed the idea that led to this paper. W.M. and Y.M. contributed to the experimental implementation and analyses. S.L. and J.A. interpreted the results. F.L. and B.L. provided critical data and contributed to the final revision of the paper. All authors have read and agreed to the published version of the manuscript.

Funding: This work was supported by the National Natural Science Foundation of China (Grant Nos. 41776195, 41941010, 42171141).

Institutional Review Board Statement: Not applicable.

Informed Consent Statement: Not applicable.

Data Availability Statement: The ALOS PALSAR data sets are provided by JAXA/METI through the services of the ASF DAAC, and the data can be found here: <https://vertex.daac.asf.alaska.edu/> (accessed on 12 February 2020). The MEaSURES BedMachine Antarctica (Version 2) data sets are openly available in National Snow and Ice Data Center at <https://doi.org/10.5067/E1QL9HFQ7A8M> (accessed on 12 February 2020).

Acknowledgments: The authors are very grateful to the JAXA/METI and ASF DAAC for providing ALOS-1 data, and to the National Snow and Ice Data Center for providing MEaSURES BedMachine Antarctica (Version 2) dataset.

Conflicts of Interest: The authors declare no conflict of interest.

References

1. Chen, Y.; Zhou, C.; Ai, S.; Liang, Q.; Zheng, L.; Liu, R.; Lei, H. Dynamics of Dalk Glacier in East Antarctica Derived from Multisource Satellite Observations Since 2000. *Remote Sens.* **2020**, *12*, 1809. [[CrossRef](#)]
2. Zhong, X.; Kang, S.; Guo, W.; Chen, J. The rapidly shrinking cryosphere in the past decade: An interpretation of cryospheric changes from IPCC WGI Sixth Assessment Report. *J. Glaciol. Geocryol.* **2021**, *12*, 1–8. [[CrossRef](#)]
3. Gardner, A.S.; Moholdt, G.; Scambos, T.; Fahnestock, M.; Ligtenberg, S.; Broeke, M.V.D.; Nilsson, J. Increased West Antarctic and unchanged East Antarctic ice discharge over the last 7 years. *Cryosphere* **2018**, *12*, 521–547. [[CrossRef](#)]
4. Tomar, K.S.; Kumari, S.; Luis, A.J. Seasonal Ice Flow Velocity variations of Polar Record Glacier, East Antarctica during 2016–2019 using Sentinel-1 data. *Geocarto Int.* **2021**, 1–14. [[CrossRef](#)]
5. Liang, Q.; Zhou, C.; Howat, I.M.; Jeong, S.; Liu, R.; Chen, Y. Ice flow variations at Polar Record Glacier, East Antarctica. *J. Glaciol.* **2019**, *65*, 279–287. [[CrossRef](#)]
6. Joughin, I.; Smith, B.E.; Abdalati, W. Glaciological advances made with interferometric synthetic aperture radar. *J. Glaciol.* **2010**, *56*, 1026–1042. [[CrossRef](#)]
7. Shen, Q.; Wang, H.; Shum, C.K.; Jiang, L.; Hsu, H.T.; Dong, J. Recent high-resolution Antarctic ice velocity maps reveal increased mass loss in Wilkes Land, East Antarctica. *Sci. Rep.* **2018**, *8*, 1–8. [[CrossRef](#)]
8. Dirscherl, M.; Dietz, A.J.; Dech, S.; Kuenzer, C. Remote sensing of ice motion in Antarctica—A review. *Remote Sens. Environ.* **2019**, *237*, 111595. [[CrossRef](#)]
9. Andersen, J.K.; Kusk, A.; Boncori, J.P.M.; Hvidberg, C.S.; Grinsted, A. Improved Ice Velocity Measurements with Sentinel-1 TOPS Interferometry. *Remote Sens.* **2020**, *12*, 2014. [[CrossRef](#)]
10. Rignot, E.; Mouginot, J.; Scheuchl, B. Ice Flow of the Antarctic Ice Sheet. *Science* **2011**, *333*, 1427–1430. [[CrossRef](#)] [[PubMed](#)]
11. Lei, Y.; Gardner, A.; Agram, P. Autonomous Repeat Image Feature Tracking (autoRIFT) and Its Application for Tracking Ice Displacement. *Remote Sens.* **2021**, *13*, 749. [[CrossRef](#)]
12. Lee, C.-K.; Seo, K.-W.; Han, S.-C.; Yu, J.; Scambos, T.A. Ice velocity mapping of Ross Ice Shelf, Antarctica by matching surface undulations measured by ICESat laser altimetry. *Remote Sens. Environ.* **2012**, *124*, 251–258. [[CrossRef](#)]

13. Liao, H.; Meyer, F.J.; Scheuchl, B.; Mouginot, J.; Joughin, I.; Rignot, E. Ionospheric correction of InSAR data for accurate ice velocity measurement at polar regions. *Remote Sens. Environ.* **2018**, *209*, 166–180. [[CrossRef](#)]
14. Mouginot, J.; Scheuchl, B.; Rignot, E. Mapping of Ice Motion in Antarctica Using Synthetic-Aperture Radar Data. *Remote Sens.* **2012**, *4*, 2753–2767. [[CrossRef](#)]
15. Chae, S.-H.; Lee, W.-J.; Jung, H.-S.; Zhang, L. Ionospheric Correction of L-Band SAR Offset Measurements for the Precise Observation of Glacier Velocity Variations on Novaya Zemlya. *IEEE J. Sel. Top. Appl. Earth Obs. Remote Sens.* **2017**, *10*, 3591–3603. [[CrossRef](#)]
16. Zhou, C.; Deng, F.; Chen, Y.; Wang, Z. Ice-flow Features in the Grove Mountations Area Using SAR Data. *Geomat. Inf. Sci. Whuhan Univ.* **2015**, *40*, 1428–1433.
17. Kimura, H.; Andoh, T. Ionospheric effects correction of ALOS PALSAR interferometry in Antarctica. *Asia-Pac. Conf. Synth. Aperture Radar* **2013**, *1*, 188–191.
18. Zhu, W.; Ding, X.L.; Jung, H.S.; Zhang, Q.; Zhang, B.C.; Qu, W. Investigation of ionospheric effects on SAR Interferometry (InSAR): A case study of Hong Kong. *Adv. Space Res.* **2016**, *58*, 564–576. [[CrossRef](#)]
19. Gomba, G.; Parizzi, A.; De Zan, F.; Eineder, M.; Bamler, R. Toward Operational Compensation of Ionospheric Effects in SAR Interferograms: The Split-Spectrum Method. *IEEE Trans. Geosci. Remote Sens.* **2015**, *54*, 1446–1461. [[CrossRef](#)]
20. Li, B.; Wang, Z.; An, J.; Zhang, B.; Geng, H.; Ma, Y.; Li, M.; Qian, Y. Ionospheric Phase Compensation for InSAR Measurements Based on the Faraday Rotation Inversion Method. *Sensors* **2020**, *20*, 6877. [[CrossRef](#)]
21. Gomba, G.; Gonzalez, F.R.; De Zan, F. Ionospheric Phase Screen Compensation for the Sentinel-1 TOPS and ALOS-2 ScanSAR Modes. *IEEE Trans. Geosci. Remote Sens.* **2016**, *55*, 223–235. [[CrossRef](#)]
22. Liang, C.; Agram, P.; Simons, M.; Fielding, E.J. Ionospheric Correction of InSAR Time Series Analysis of C-band Sentinel-1 TOPS Data. *IEEE Trans. Geosci. Remote Sens.* **2019**, *57*, 6755–6773. [[CrossRef](#)]
23. Milczarek, W.; Kopeć, A.; Głabicki, D. Estimation of Tropospheric and Ionospheric Delay in DInSAR Calculations: Case Study of Areas Showing (Natural and Induced) Seismic Activity. *Remote Sens.* **2019**, *11*, 621. [[CrossRef](#)]
24. Brcic, R.; Parizzi, A.; Eineder, M.; Bamler, R.; Meyer, F. Estimation and compensation of ionospheric delay for SAR interferometry. In Proceedings of the 2010 IEEE International Geoscience and Remote Sensing Symposium, Honolulu, HI, USA, 25–30 July 2010; pp. 2908–2911.
25. Mao, W.; Liu, G.; Wang, X.; Zhang, R.; Xiang, W.; Wu, S.; Zhang, B.; Bao, J.; Cai, J.; Pirasteh, S. An InSAR Ionospheric Correction Method Based on Variance Component Estimation With Integration of MAI and RSS Measurements. *IEEE J. Sel. Top. Appl. Earth Obs. Remote Sens.* **2020**, *14*, 1423–1433. [[CrossRef](#)]
26. Hasni, K.; Chen, J.; Zhuo, L. A Refined Split-Spectrum Algorithm for Correcting Ionospheric Effects on Interferograms of Spaceborne D-InSAR at Longer Wavelength. In Proceedings of the IEEE International Geoscience and Remote Sensing Symposium, Beijing, China, 10–15 July 2016.
27. Fattahi, H.; Simons, M.; Agram, P. InSAR Time-Series Estimation of the Ionospheric Phase Delay: An Extension of the Split Range-Spectrum Technique. *IEEE Trans. Geosci. Remote Sens.* **2017**, *55*, 5984–5996. [[CrossRef](#)]
28. Liao, H.; Meyer, F.J. A combined estimator for Interferometric SAR ionosphere correction. In Proceedings of the 2016 IEEE International Geoscience and Remote Sensing Symposium (IGARSS), Beijing, China, 1–15 July 2016; IEEE: Piscataway, NJ, USA, 2016; pp. 6499–6501.
29. Wegmüller, U.; Werner, C.; Frey, O.; Magnard, C.; Strozzi, T. Reformulating the Split-Spectrum Method to Facilitate the Estimation and Compensation of the Ionospheric Phase in SAR Interferograms. *Procedia Comput. Sci.* **2018**, *138*, 318–325. [[CrossRef](#)]
30. Dou, F.; Lv, X.; Chen, Q.; Sun, G.; Yun, Y.; Zhou, X. The Impact of SAR Parameter Errors on the Ionospheric Correction Based on the Range-Doppler Model and the Split-Spectrum Method. *Remote Sens.* **2020**, *12*, 1607. [[CrossRef](#)]
31. Raucoules, D.; De Michele, M. Assessing Ionospheric Influence on L-Band SAR Data: Implications on Coseismic Displacement Measurements of the 2008 Sichuan Earthquake. *IEEE Geosci. Remote Sens. Lett.* **2009**, *7*, 286–290. [[CrossRef](#)]
32. Kim, J.S.; Papathanassiou, K.P.; Scheiber, R.; Quegan, S. Correcting Distortion of Polarimetric SAR Data Induced by Ionospheric Scintillation. *IEEE Trans. Geosci. Remote Sens.* **2015**, *53*, 6319–6335.
33. Fretwell, P.; Pritchard, H.D.; Vaughan, D.G.; Bamber, J.L.; Barrand, N.E.; Bell, R.; Bianchi, C.; Bingham, R.G.; Blankenship, D.D.; Casassa, G.; et al. Bedmap2: Improved ice bed, surface and thickness datasets for Antarctica. *Cryosphere* **2013**, *7*, 375–393. [[CrossRef](#)]
34. Liu, Z.; Jung, H.-S.; Lu, Z. Joint Correction of Ionosphere Noise and Orbital Error in L-Band SAR Interferometry of Interseismic Deformation in Southern California. *IEEE Trans. Geosci. Remote Sens.* **2013**, *52*, 3421–3427. [[CrossRef](#)]
35. Zhang, B.; Ding, X.; Zhu, W. An Asymmetric Split-Spectrum Method for Estimating the Ionospheric Artifacts in InSAR Data. In Proceedings of the IEEE International Geoscience and Remote Sensing Symposium, Valencia, Spain, 22–27 July 2018.
36. Setiawan, N.; Furuya, M. Tropospheric dispersive phase anomalies during heavy rain detected by L-band InSAR and their interpretation. *Earth Planets Space* **2021**, *73*, 1–14. [[CrossRef](#)]
37. Kim, J.S.; Danklmayer, A.; Papathanassiou, K. Correction of ionospheric distortions in low frequency interferometric SAR data. In Proceedings of the 2011 IEEE International Geoscience and Remote Sensing Symposium, Vancouver, BC, Canada, 24–29 July 2011. [[CrossRef](#)]
38. Gomba, G.; De Zan, F. Bayesian Data Combination for the Estimation of Ionospheric Effects in SAR Interferograms. *IEEE Trans. Geosci. Remote Sens.* **2017**, *55*, 6582–6593. [[CrossRef](#)]

39. Ning, J.; Wang, R.; Wang, J.; Zhang, B.; Zhao, S. Ionospheric correction of ALOS-2 full-aperture ScanSAR interferometric data for surface deformation measurement in Beijing. *J. Eng.* **2019**, *2019*, 5685–5688. [[CrossRef](#)]
40. Wang, N.; Fu, H.; Li, S.; Xu, F. Retrieving ionospheric TEC based on the split-spectrum method. *J. Terahertz Sci. Electron. Inf. Technol.* **2017**, *15*, 198–205. [[CrossRef](#)]
41. Bamler, R.; Eineder, M. Accuracy of Differential Shift Estimation by Correlation and Split-Bandwidth Interferometry for Wideband and Delta-k SAR Systems. *IEEE Geosci. Remote Sens. Lett.* **2005**, *2*, 151–155. [[CrossRef](#)]
42. Meyer, F.J. Performance Requirements for Ionospheric Correction of Low-Frequency SAR Data. *IEEE Trans. Geosci. Remote Sens.* **2011**, *49*, 3694–3702. [[CrossRef](#)]
43. Cheng, X.; Zhang, Y. Detecting Ice Motion with Repeat-pass ENVISAT ASAR Interferometry over Nunataks Region in Grove Mountain, East Antarctic-The Preliminary Result. *J. Remote Sens.* **2006**, *10*, 5186–5189.
44. Zeng, Z.; Wang, Z.; Ding, M.; Zheng, X.; Sun, X.; Zhu, W.; Zhu, K.; An, J.; Zang, L.; Guo, J.; et al. Estimation and Long-term Trend Analysis of Surface Solar Radiation in Antarctica: A Case Study of Zhongshan Station. *Adv. Atmos. Sci.* **2021**, *38*, 1497–1509. [[CrossRef](#)]
45. Chunxia, Z.; Dongchen, E.; Mingsheng, L. Feasibility of InSAR Application to Antarctic Mapping. *Geomat. Inf. Sci. Wuhan Univ.* **2004**, *29*, 619–623.
46. Joughin, I. Ice-sheet velocity mapping: A combined interferometric and speckle-tracking approach. *Ann. Glaciol.* **2002**, *34*, 195–201. [[CrossRef](#)]
47. Zheng, W.; Hu, J.; Liu, J.; Sun, Q.; Li, Z.; Zhu, J.; Wu, L. Mapping Complete Three-Dimensional Ice Velocities by Integrating Multi-Baseline and Multi-Aperture InSAR Measurements: A Case Study of the Grove Mountains Area, East Antarctic. *Remote Sens.* **2021**, *13*, 643. [[CrossRef](#)]
48. Mouginot, J.; Rignot, E.; Scheuchl, B.; Millan, R. Comprehensive Annual Ice Sheet Velocity Mapping Using Landsat-8, Sentinel-1, and RADARSAT-2 Data. *Remote Sens.* **2017**, *9*, 364. [[CrossRef](#)]